Transformation acoustics with bulk media composed of polarized sources

Dylan A. Kovacevich [*] and Bogdan-Ioan Popa[†]

Department of Mechanical Engineering, University of Michigan, Ann Arbor, Michigan 48109, USA

Active acoustic metamaterials consisting of paired sensor-driver unit cells offer a promising path towards the practical realization of exciting transformation acoustics devices. The design of these cells is founded in a microscopic acoustic model that describes materials as collections of subwavelength polarized sources which respond to the local conditions of pressure and particle velocity. The current ability to express the polarizabilities that characterize these sources in terms of the effective macroscopic acoustic properties is limited to only a few simple cases and is not applicable to inhomogeneous bulk media of arbitrary geometries. Here, we address this challenge and derive general closed-form expressions relating the bulk modulus to the monopole polarizability and the mass density tensor to the dipole polarizability. Furthermore, we use these expressions to adapt transformation acoustics to the microscopic model. We demonstrate the accuracy of our approach by comparing the fields scattered by several devices, including cylindrical cloaks with steep property gradients and anisotropy, with the fields scattered by the devices' realizations with polarized sources.

I. INTRODUCTION

Transformation acoustics has enabled the design of devices that exhibit remarkable behavior, but in turn have demanding material property requirements, such as steep gradients and anisotropy [1–3]. The ability to physically realize these devices is limited, as the prescribed property distributions cannot be obtained with conventional materials. The development of passive metamaterials, artificial materials composed of subwavelength engineered unit cells, has expanded the accessible design space beyond what nature offers. Wide control over the bulk modulus and mass density, even into the negative regime, has been demonstrated with passive acoustic metamaterials composed of cavity resonators [4], tubes with side holes [5], coated beads [6,7], membranes [8,9], and space-coiling structures [10,11]. Anisotropy and spatially varying properties can be achieved by tuning the geometries of these components [12–15]. However, most passive metamaterials require resonances to realize the acoustic properties specified by transformation acoustics. Therefore, they are narrow band and unsuitable for ubiquitous acoustics applications such as noise mitigation, sonar, and ultrasound imaging, which require the manipulation of broadband sound. In addition, the reliance on resonance, undesirable coupling of properties, and general challenges in manufacturing are substantial obstacles to precise control of the properties and constrain the operating conditions [16–18].

The shortcomings of passive acoustic metamaterials are reflected in the transformation acoustics devices demonstrated so far. Despite being one of the most sought after transformation acoustics structures, omnidirectional cloaking shells have only been accomplished in cases of reduced geometric and material complexity, as in carpet cloaks [19–21], and through approximations of the prescribed material properties that are suitable only for devices of less than several wavelengths in diameter [14,22,23].

Active metamaterials, which feature a programed response dependent on the external conditions, may provide a path to overcome many of the inherent constraints of passive structures. Particularly promising are unit cells consisting of sensor-driver pairs, which were first conceived for manipulating electromagnetic fields [24], but were later applied to control acoustic and elastic waves [25–36]. Sensor-driver cells sense the impinging external field and generate a coherent acoustic field in response. Consequently, it has been shown [33,34] that media based on these types of cells could be realized by leveraging a microscopic model of matter or source-driven homogenization theory [37–41]. In this model, the behavior of a continuous material can be represented by the collective response of numerous pointlike sources placed in a background medium and separated by significantly subwavelength distances. These sources generate either monopole or dipole fields and are characterized by their polarizabilities, which relate the source amplitudes to the local fields. In the case of acoustics of typical materials, the monopole moment depends on the local acoustic pressure and the dipole moment depends on the local particle velocity. The polarizabilities of these sources depend on the macroscopic acoustic properties of bulk modulus and mass density, respectively.

For application in active metamaterials, a sensor-driver cell is equivalent to a polarized microscopic source, and the electronic transfer function from the sensor input to the driver output is proportional to the polarizability. In principle, the monopole and dipole transfer functions of the active cell could be tuned independently to yield desired macroscopic

─────────
[*]dkovac@umich.edu
[†]bipopa@umich.edu

properties [33–36]. However, one major obstacle here is that there is no general method for determining the polarizabilities that correspond to a given set of macroscopic material properties, especially in scenarios involving inhomogeneous bulk media of arbitrary geometries. Previous works have mostly focused on Willis media, with analytical solutions only having been found in a few limited cases, such as homogeneous materials implemented with one-dimensional (1D) periodic lattices [42], homogeneous one cell thick metasurfaces [43], and subwavelength resonators [43,44].

In this work, we address the challenge of obtaining expressions for the polarizabilities necessary to model bulk media of arbitrary geometry and macroscopic acoustic properties, in particular the inhomogeneous, highly anisotropic media required by transformation acoustics. While we are motivated by the physical realization of active metamaterials, we focus here on establishing a more general theory applicable to active and passive media rather than the specifics of such an implementation. First, in Sec. II, we develop a model of a unit cell composed of three collocated polarized sources and analyze its interactions with the impinging local acoustic field. Then, we relate the cell's response to an external plane wave with the scattered field from a subwavelength anisotropic cylinder. This leads to expressions for the polarizabilities as functions of the macroscopic properties of the cylinder and, ultimately, the effective properties of a homogenized metamaterial consisting of a lattice of cylinders. Although the polarizability relationships we obtained are for a two-dimensional (2D) space, the expressions in a three-dimensional (3D) space can be obtained by substitution of the cylinder-based model with a sphere-based one. Lastly, we write a system of equations to determine the source amplitudes of a lattice of unit cells given the source polarizabilities and the external field. In Sec. III, we demonstrate the ability to model a finite homogeneous slab of given bulk modulus and isotropic mass density as a lattice of unit cells. The results are validated through comparisons with finite element method (FEM) simulations using COMSOL MULTIPHYSICS. Finally, in Sec. IV, we adapt the transformation acoustics equations to directly provide closed-form expressions for the polarizabilities and simulate several omnidirectional free space cloaks, highlighting the capability to accurately represent the most challenging material properties prescribed by transformation acoustics.

II. UNIT CELL MODEL

In the microscopic acoustic model [42], a material can be represented as a lattice of subwavelength sources that each generate a response to the local conditions based on their polarizability. Here, we consider square and hexagonal lattices of unit cells in a 2D space, and define a single cell in an inviscid background fluid as a group of collocated line sources whose amplitudes depend on the local pressure and particle velocity. The sources include one monopole and two dipoles aligned along the Cartesian axes. The dipoles can be further decomposed as a pair of fully out of phase monopoles separated by an infinitesimal distance 2δ, as illustrated in Fig. 1(a). We will show next that this cell structure can realize the most demanding acoustic material parameters required by
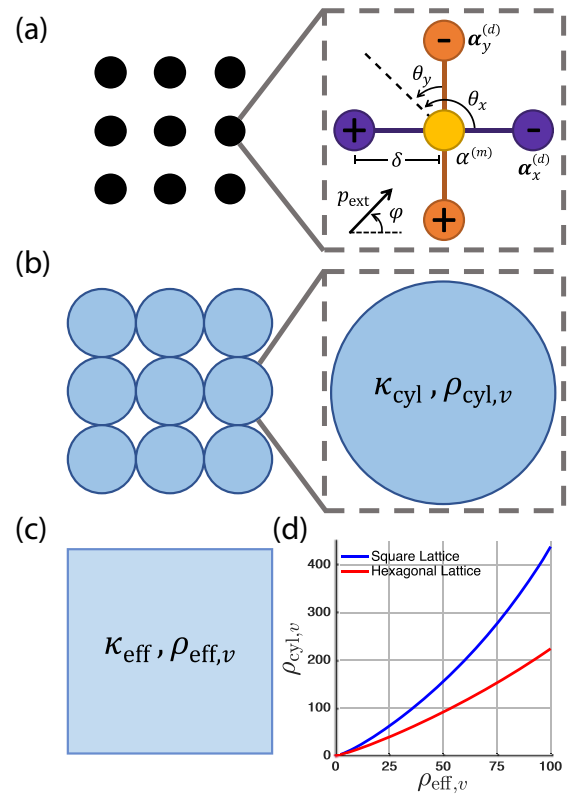

FIG. 1. Diagram of modeling a continuous material as a lattice of unit cells. (a) The unit cells consist of three polarized sources, one monopole and two dipoles, in each of the Cartesian directions. (b) Each cell is equivalent to a subwavelength anisotropic cylinder of uniform macroscopic bulk modulus $\kappa_{\rm cyl}$ and diagonal mass density tensor components $\rho_{{\rm cyl},v}$ with $v \in \{x, y\}$. (c) The array of cylinders and background fluid are homogenized as a continuous block of material with effective macroscopic properties. (d) The relationships of the mass densities of (b) and (c) obtained in FEM simulations.

transformation acoustics including high mass anisotropy and large gradient bulk modulus and density profiles.

The response of a unit cell is characterized by a scalar monopole polarizability $\alpha^{(m)}$ and tensor dipole polarizability $\boldsymbol{\alpha}^{(d)}$, which relate the amplitude of the acoustic response to the local conditions of pressure $p_{\rm loc}$ and particle velocity $\bar{u}_{\rm loc}$, respectively. Works concerning Willis media include cross polarizabilities between the monopole and dipole components, but we are only concerned with typical media, so they will be neglected here. Additionally, there are several normalizations of the monopole and dipole moments that have been previously used, such as by the macroscopic properties [42] or a unit volume [43], but we simply consider amplitudes of line sources to be defined later in Eqs. (3). We write the monopole amplitude $A^{(m)}$ and dipole amplitudes $A_x^{(d)}$ and $A_y^{(d)}$ dependent on the local conditions as

$$A^{(m)} = \alpha^{(m)} p_{\rm loc}, \quad \begin{bmatrix} A_x^{(d)} \\ A_y^{(d)} \end{bmatrix} = \begin{bmatrix} \alpha_x^{(d)} & 0 \\ 0 & \alpha_y^{(d)} \end{bmatrix} \begin{bmatrix} u_{{\rm loc},x} \\ u_{{\rm loc},y} \end{bmatrix}. \quad (1)$$

As typically considered in the microscopic model, the local conditions, $p_{\rm loc}$ and $\bar{u}_{\rm loc}$, include the external fields and acoustic responses of other cells, but not the response of the cell for which Eqs. (1) are written. The dipole polarizability tensor

here is diagonal, indicating that a dipole oriented along the v axis (where v is either x or y) is sensitive to the particle velocity component along the same v axis, namely the principal axes of the cell coincide with the Cartesian axes. In the case where $\alpha_x^{(d)} \neq \alpha_y^{(d)}$, the cell is anisotropic. The nondiagonal $\boldsymbol{\alpha}^{(d)}$ will be discussed in Sec. IV.

Our analysis will pursue the following steps. First, as an intermediary to determine the relationship between the macroscopic properties and the microscopic polarizabilities, we will show that each unit cell scatters sound identically, even in the near field, to an acoustically small cylinder of radius $a \ll \lambda$, where λ is the wavelength. This important observation will allow us to replace the cell sources with a homogeneous cylinder with mass density and bulk modulus expressed in terms of the source polarizabilities and lattice geometry. The equivalency of the sources and cylinder is shown in Fig. 1(b) at both the lattice and unit cell level. Second, using homogenization techniques, we will relate the properties of cylinders in a lattice surrounded by background fluid to the properties of a continuous material, as in Fig. 1(c). Finally, we will directly determine the polarizabilities from the effective macroscopic properties.

To compare the behavior of a cell and cylinder, we analyze the simple case of a plane wave of arbitrary direction incident on a single unit cell. The relationship found in this study should then be valid for any general field, including the complex field scattered by a large lattice of cells, because in linear acoustics all complex fields can be decomposed into a superposition of plane waves. Throughout this work we assume a harmonic regime and $e^{j\omega t}$ time variation, where ω is the angular frequency. The pressure p_{ext} and particle velocity $\bar{u}_{\text{ext}}$ of an incident plane wave propagating at the angle φ relative to the x axis are expressed as

$$p_{\text{ext}} = P_0 e^{-jk_0(x\cos\varphi + y\sin\varphi)},$$
$$\bar{u}_{\text{ext}} = \hat{k}\frac{P_0}{z_0} e^{-jk_0(x\cos\varphi + y\sin\varphi)}, \tag{2}$$

where P_0 is the pressure amplitude and z_0 is the characteristic impedance of the background fluid. The wave vector of this plane wave is determined by the background fluid wave number k_0 and the unit vector $\hat{k} = \hat{x}\cos\varphi + \hat{y}\sin\varphi$, with $\hat{x}$ and $\hat{y}$ being the Cartesian basis vectors.

The general acoustic pressure expressions of the waves launched by the monopole and dipole sources are written in terms of Hankel functions [45],

$$p^{(m)} = A^{(m)} H_0^{(2)}(k_0 r),$$
$$p_v^{(d)} = \frac{A_v^{(d)}}{k_0\delta}\left[H_0^{(2)}(k_0 r_{v+}) - H_0^{(2)}(k_0 r_{v-})\right]$$
$$= A_v^{(d)}(2\cos\theta_v)H_1^{(2)}(k_0 r), \tag{3}$$

where r and θ_v are the polar coordinates of the location where the fields are evaluated relative to the center of the cell. The angle θ_v is relative to the orientation of the dipole pointing along the v axis with $v \in \{x, y\}$ [see Fig. 1(a)]. The acoustic pressure launched by the dipole can be written as the summed pressures of two monopole sources located at $\pm\delta$ along the axis, shown in the second line of Eq. (3), or as the simplified expression shown beneath. Although the simplified version is

enough for the theoretical analysis of this section, the first form is more useful in the numerical simulations and in view of the physical realization of the dipoles. In the above expressions, the distances between the monopole sources forming the dipole and the location where the fields are evaluated are denoted r_{v+} and r_{v-}.

The total pressure p_{uc} launched by the isolated unit cell responding to the plane wave given in Eq. (2) can then be written as the sum of the source components,

$$p_{\text{uc}} = p^{(m)} + p_x^{(d)} + p_y^{(d)}, \tag{4}$$

where the monopole and dipole acoustic pressures are given by Eq. (3) in which $A^{(m)}$ and $A_v^{(d)}$ are provided by Eq. (1) with $p_{\text{loc}} = p_{\text{ext}}$ and $\bar{u}_{\text{loc}} = \bar{u}_{\text{ext}}$. We parametrize θ_v in one variable θ such that $\theta_x = \theta$ and $\theta_y = \theta - \frac{\pi}{2}$ to obtain the expressions of the monopole and dipole pressures appearing in the above equation as

$$p^{(m)} = \alpha^{(m)} P_0 H_0^{(2)}(k_0 r),$$
$$p_x^{(d)} = \alpha_x^{(d)}\frac{P_0}{z_0}\cos\varphi(2\cos\theta)H_1^{(2)}(k_0 r),$$
$$p_y^{(d)} = \alpha_y^{(d)}\frac{P_0}{z_0}\sin\varphi(2\sin\theta)H_1^{(2)}(k_0 r). \tag{5}$$

We will now compare p_{uc} with the scattered field from the plane wave of Eq. (2) incident on an anisotropic cylinder of radius a, relative bulk modulus κ_{cyl}, and relative mass density tensor $\boldsymbol{\rho}_{\text{cyl}}$. In this work, the relative material properties are normalized to the properties of the background fluid. It has recently been shown that the acoustic pressure scattered by this anisotropic cylinder can be written as an infinite sum of Bessel-like functions [46]. For acoustically small cylinders, where $a \ll \lambda$, only the first three terms corresponding to the monopole and dipole moments dominate and the scattered pressure field assumes the closed-form expression

$$p_{\text{cyl}} = B_0 P_0 H_0^{(2)}(k_0 r)$$
$$+ B_{1,x} P_0 \cos\varphi(2\cos\theta)H_1^{(2)}(k_0 r)$$
$$+ B_{1,y} P_0 \sin\varphi(2\sin\theta)H_1^{(2)}(k_0 r), \tag{6}$$

where

$$B_0 = j(k_0 a)^2\frac{\pi}{4}\left[1 - \frac{1}{\kappa_{\text{cyl}}}\right],$$
$$B_{1,v} = (k_0 a)^2\frac{\pi}{4}\left[\frac{1 - \rho_{\text{cyl},v}}{1 + \rho_{\text{cyl},v}}\right]. \tag{7}$$

Remarkably, the expressions of the coefficients B_0, $B_{1,x}$, and $B_{1,y}$ for the acoustically small anisotropic cylinder assume the same exact form as for an acoustically small isotropic cylinder [47]. In fact, when $\rho_{\text{cyl},x} = \rho_{\text{cyl},y}$, Eqs. (6) and (7) reduce to the expression derived for an isotropic cylinder [47].

By comparing the scattered field expressions for the unit cell in Eqs. (4) and (5) and subwavelength anisotropic cylinder in Eq. (6), we can relate the polarizabilities to the coefficients B_0 and $B_{1,v}$,

$$\alpha^{(m)} = B_0,$$
$$\alpha_v^{(d)} = z_0 B_{1,v}, \tag{8}$$

giving us a direct relationship between the polarizabilities and the macroscopic cylinder properties.

We have now established that a subwavelength cylinder can serve as an analog of the unit cell formed by polarized sources shown in Fig. 1(a). Therefore, an array of these cells scatters sound like an array of cylinders [Fig. 1(b)]. Because the cylinders are highly subwavelength, the first order approximation presented in Eq. (6) is sufficient to characterize their response regardless of their orientation and proximity in an array. Next, we homogenize the lattice of cylinders and background fluid such that it is equivalent to a continuous material of relative effective properties κ_{eff} and $\rho_{\text{eff},v}$, as shown in Fig. 1(c).

Since the compliance of mixes of two fluids is the average of the fluid compliances [46], we obtain a closed-form relationship between κ_{eff} and κ_{cyl}, namely

$$\kappa_{\text{cyl}}^{-1} = f^{-1}\left(\kappa_{\text{eff}}^{-1} - 1\right) + 1, \tag{9}$$

where f is the filling fraction. Homogenizing the mass density is more involved. One standard approach is to send plane waves in the x and y directions through a lattice of cylinders and to obtain the effective densities along these axes from reflection and transmission coefficient simulations [13,48]. This numerical method produces the mapping between the effective and cylinder mass densities along the x and y axes,

$$\rho_{\text{cyl},v} = g(\rho_{\text{eff},v}), \tag{10}$$

where v represents any of the Cartesian axes x or y. The mapping g is shown in Fig. 1(d) with solid lines for two cylinder lattices (square and hexagonal). We conducted the simulation in COMSOL with highly subwavelength cylinders packed at a maximum density in the specified arrangement. This simulation approach has been described in detail in [13] and has been used successfully to design and characterize various metamaterial devices [15,20,29]. A closed-form expression of the mapping in Eq. (10) can be obtained by fitting the numerically simulated g [49]. The result is independent of the cylinder radius, given that the unit cells are subwavelength and the filling fraction is fixed.

We note that the component $\rho_{\text{cyl},v}$ depends only on $\rho_{\text{eff},v}$ and not on the mass density component in the direction perpendicular to v. This can be explained by Eqs. (7), where it is evident that the strength of the dipole along the direction v for an acoustically small anisotropic cylinder depends only on the mass density component along v.

Combining Eqs. (7) to (10), we can finally write the polarizabilities directly as functions of the effective macroscopic properties:

$$\alpha^{(m)} = jf^{-1}(k_0 a)^2 \frac{\pi}{4}\left(1 - \frac{1}{\kappa_{\text{eff}}}\right),$$

$$\alpha_v^{(d)} = z_0(k_0 a)^2 \frac{\pi}{4}\left[\frac{1 - g(\rho_{\text{eff},v})}{1 + g(\rho_{\text{eff},v})}\right]. \tag{11}$$

Now, we develop a method for finding the amplitudes of the numerous interacting sources in the lattice that represents a continuous material. The response of a single source is derived from both the external waves and the contributions of all of the other sources. The amplitudes of the sources in the ith unit cell

in a set of N total cells can be written as

$$A_i^{(m)} = \alpha_i^{(m)}\left[p_{\text{ext}} + \sum_{\substack{n=1 \\ n \neq i}}^{N}\left(p_n^{(m)} + p_{n,x}^{(d)} + p_{n,y}^{(d)}\right)\right],$$

$$A_{i,v}^{(d)} = \alpha_{i,v}^{(d)}\left[u_{\text{ext},v} + \sum_{\substack{n=1 \\ n \neq i}}^{N}\left(u_{n,v}^{(m)} + u_{n,xv}^{(d)} + u_{n,yv}^{(d)}\right)\right], \tag{12}$$

where $p_n^{(m)}$, $p_{n,x}^{(d)}$, and $p_{n,y}^{(d)}$ are the acoustic pressures produced by the monopole and dipoles oriented along the x and y directions of the nth cell at the position of the ith cell. They are given by Eqs. (3), in which r is the distance between the centers of the ith and nth cell. Similarly, $u_{n,v}^{(m)}$ represents the v component of the particle velocities produced by the monopole source and $u_{n,wv}^{(d)}$ represents the v component of the particle velocity produced by the dipole oriented along the w axis of the nth cell at the position of the ith cell. Here, both v and w can be either of the x and y axes. The expressions of these velocities are given below:

$$u_{n,v}^{(m)} = \frac{A_n^{(m)}}{jz_0}(\hat{r} \cdot \hat{v})H_1^{(2)}(k_0 r),$$

$$u_{n,wv}^{(d)} = \frac{jA_{n,w}^{(d)}}{k_0 z_0}\left\{(\hat{r} \cdot \hat{v})k_0 \cos\theta_w\left[H_0^{(2)}(k_0 r) - H_2^{(2)}(k_0 r)\right]\right.$$

$$\left. - (\hat{\theta}_w \cdot \hat{v})\frac{2}{r}\sin\theta_w\left[H_1^{(2)}(k_0 r)\right]\right\}. \tag{13}$$

In these equations, the v component of the particle velocity is found from the dot product of the Cartesian basis vector $\hat{v}$ with the source velocity vector, which is expressed using the polar basis vectors $\hat{r}$ and $\hat{\theta}_w$.

This allows for a system of equations to be written from which all of the source amplitudes can be solved for given their polarizabilities and the external impinging field. A general expression of this system is

$$E_k = \sum_{j=1}^{3N} C_{kj} A_j, \tag{14}$$

where C_{kj} is a square matrix of dimension $3N$ that encompasses the source interactions, E_k is a column matrix of the external field sensed at each source, and A_j is a column matrix of the source amplitudes we want to determine. The source amplitudes are ordered such that every set of three (one monopole and two dipoles) corresponds to the same unit cell. Consequently, 3×3 submatrices along the diagonal of C_{kj} represent interactions of sources within the same unit cell. In our model, we assume that there is no intracell feedback or, in other words, the response of a cell is not coupled with its own field. As a result, these submatrices will each be set as the identity matrix.

In summary, a continuous material of arbitrary geometry with effective properties κ_{eff} and $\boldsymbol{\rho}_{\text{eff}}$ can be modeled by an array of subwavelength-spaced unit cells. Once the appropriate polarizabilities are calculated via Eqs. (11), the system
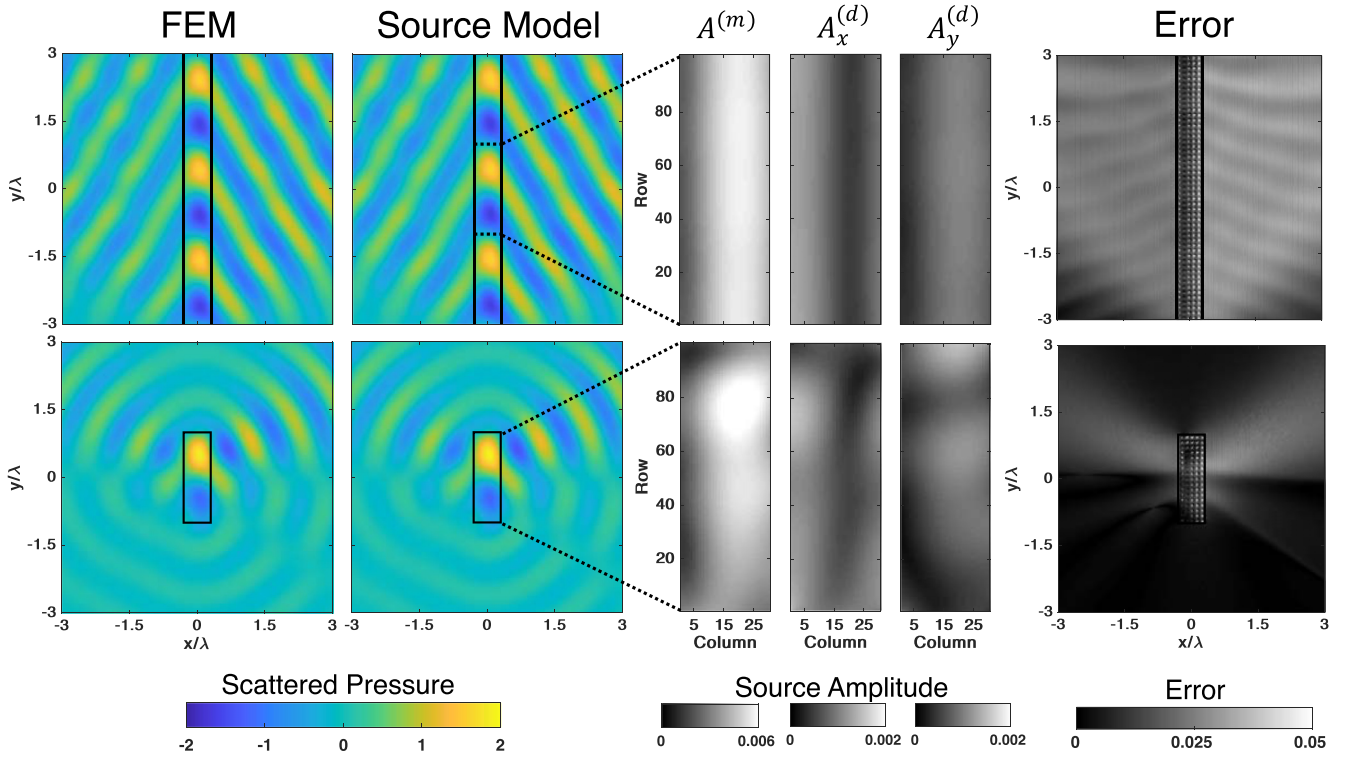
FIG. 2. Scattering from a plane wave obliquely incident on acoustically short and tall slabs (outlined in black) of $\kappa_{\text{eff}} = 3$ and $\rho_{\text{eff}} = 2$ is compared between an FEM and source model simulation. The amplitudes of the sources in the cell lattice are shown for slab sections of equal dimension. The error of the source model scattered field amplitude is plotted relative to the maximum pressure in the simulated region.

of equations shown in Eq. (14) can be solved to determine the response to a given external field. Our demonstrations of this approach will utilize both square and hexagonal lattices of cells, but any unit cell with sufficiently subwavelength dimension is viable. We will demonstrate the modeling of continuous media with rectangular and circular geometries.

III. HOMOGENEOUS ISOTROPIC SLAB

To evaluate our source model and the relationship we found between their polarizabilities and macroscopic acoustic properties, we compared our simulations of scattered pressure fields using an array of unit cells to FEM simulations of a continuous material. For the source model, the scattered field is the sum of all the source responses with amplitudes found from solving the system in Eq. (14). In the FEM simulation, it is simply the total field subtracted by the incident field.

Our first demonstration is a plane wave incident on a homogeneous isotropic slab. Oblique incidence of $30°$ was chosen so that both dipole orientations would be excited and the relative material properties $\kappa_{\text{eff}} = 3$ and $\rho_{\text{eff}} = 2$ were selected to produce significant reflected and transmitted waves. The geometry was defined in terms of the wavelength λ of the plane wave in the background fluid. We examined two slab geometries, both of width $w = 0.6\lambda$, but differing heights of $h = 2\lambda$ and $h = 8\lambda$ so that scattering dominated by diffraction/edge effects could be compared to more uniform scattering. The slabs were modeled by cells with highly subwavelength spacing of $\lambda/50$ in a square array. Because the slab is homogeneous, all of the unit cells share the same set

of polarizabilities and, because the mass density is isotropic, $\alpha_x^{(d)} = \alpha_y^{(d)}$.

The scattered fields in a 6λ by 6λ region found from both simulation methods are shown on the left in Fig. 2. The scattered fields generated by the source model closely match those found through the FEM solution of the wave equation for both geometries. This indicates that the dimension of the unit cell was sufficiently small to model the geometry and physics and that the polarizabilities were accurate representations of the macroscopic properties. The error is quantified in the rightmost plots of Fig. 2, shown as the difference in the pressure amplitudes of the FEM and source model results relative to the maximum amplitude in the domain. The high error points within the slab are a result of samples very near to the sources, where the pressure approaches infinity. Other error can be attributed to the approximations made when deriving the scattering by a cylinder from an incident plane wave. Namely, the response was assumed to be first order and for a highly subwavelength cylinder. While the tested unit cell dimension of $\lambda/50$ is subwavelength, it is not small enough for there to be no noticeable mismatch between the actual and approximated fields, especially when the error is compounded by the interactions among all of the cells. Nevertheless, the difference manifests in amplitude but not in phase and it is expected to be much smaller than the differences imposed by typical fabrication tolerances. Another way to view the error is by checking for the conservation of energy. We calculated the difference between the acoustic power entering and leaving the source model simulation domain relative to the incident power. The short slab had a 1.7% gain in power and the

tall slab had a 3.2% gain. This clarifies that there is indeed inaccuracy due to the approximated scattered fields rather than wrongly chosen polarizabilities for the desired macroscopic acoustic properties. Even so, with the intent of engineering application and physical realization, the approximations that were made and the chosen cell dimension are still a strong demonstration of the model's capabilities.

In the middle of Fig. 2 are plots of the source amplitudes in the center 2λ tall sections of both slabs. Each pixel represents a single source, with its position in the cell lattice defined by its row and column. The amplitude distributions help to visualize how the acoustic behavior is dominated by edge effects in the shorter slab, but approaches uniformity in the center of the taller slab.

While the results shown in this section are for only one set of material properties in the vicinity of the background fluid, this is not the limit of the capability of the source model. The scattered fields can be solved for more complex property distributions, as will be demonstrated for an acoustic cloak in the following section.

IV. TRANSFORMATION ACOUSTICS AND CLOAKING

Transformation acoustics enables the derivation of the bulk modulus and mass density distributions necessary to physically replicate the effects of a desired coordinate transformation. In view of the emerging active metamaterials with sensor-driver unit cells, it is useful to develop an adaptation of transformation acoustics to directly solve for the polarizabilities, rather than the macroscopic acoustic properties. We start with a general coordinate transformation given as

$$(x', y', z') = (x'(x, y, z), y'(x, y, z), z'(x, y, z)),$$

$$\mathbf{J} = \begin{bmatrix} \frac{\partial x'}{\partial x} & \frac{\partial x'}{\partial y} & \frac{\partial x'}{\partial z} \\ \frac{\partial y'}{\partial x} & \frac{\partial y'}{\partial y} & \frac{\partial y'}{\partial z} \\ \frac{\partial z'}{\partial x} & \frac{\partial z'}{\partial y} & \frac{\partial z'}{\partial z} \end{bmatrix}, \quad (15)$$

where the new primed coordinates are functions of the original nonprimed coordinates and $\mathbf{J}$ is the Jacobian matrix of the transformation. Using the linear acoustic constitutive relations for an inviscid fluid, we can then solve for the bulk modulus and mass density tensor necessary to replicate this transformation in the original coordinate system as

$$\kappa' = |\mathbf{J}|^{-1}\kappa,$$

$$\boldsymbol{\rho}' = |\mathbf{J}|^{-1}\mathbf{J}^T\boldsymbol{\rho}\mathbf{J}, \quad (16)$$

where $|\mathbf{J}|$ is the determinant of the Jacobian and $\mathbf{J}^T$ is its transpose [50]. For the source model, we assume an isotropic background fluid. Therefore, the mass density before transformation is simply $\boldsymbol{\rho} = \rho_0\mathbf{I}$, where $\mathbf{I}$ is the identity matrix. Equation (16) can now be rewritten in terms of the relative effective properties as

$$\kappa'_{\text{eff}} = |\mathbf{J}|^{-1},$$

$$\boldsymbol{\rho}'_{\text{eff}} = |\mathbf{J}|^{-1}\mathbf{J}^T\mathbf{J} = \hat{\mathbf{J}}, \quad (17)$$

with $\hat{\mathbf{J}}$ being defined for conciseness. Finally, we express these effective material properties in the principal axes, such that the mass density and Jacobian tensors are diagonal. Employing

the superscript star (*) to represent a tensor evaluated in a coordinate system in which the tensor is diagonal (i.e., the principal axis system), we use Eqs. (11) to substitute the polarizabilities for the macroscopic properties. Consequently, the transformation acoustics expressions become

$$\alpha^{(m)} = jf^{-1}(k_0 a)^2 \frac{\pi}{4}(1 - |\mathbf{J}|),$$

$$\alpha_v^{(d)} = z_0(k_0 a)^2 \frac{\pi}{4}\left[\frac{1 - g(\hat{J}_v^*)}{1 + g(\hat{J}_v^*)}\right]. \quad (18)$$

Therefore, each diagonal element of the dipole polarizability tensor indexed by v is solved for independently.

A free space cylindrical cloaking shell is a good transformation acoustics device to demonstrate the capability of microscopic modeling, as steep property gradients and anisotropy are required. One set of solutions can be found from a coordinate transformation in the radial direction from r to r' [2],

$$r' = \frac{R_2 - R_1}{R_2}r + R_1, \quad \phi' = \phi, \quad (19)$$

where R_1 is the inner radius and R_2 is the outer radius of the shell. The resultant radially varying mass density and inverse bulk modulus are according to Eq. (16) and [2]

$$\rho'_r = \frac{r'}{r' - R_1}, \quad \rho'_\phi = \frac{r' - R_1}{r'},$$

$$(\kappa')^{-1} = \left(\frac{R_2}{R_2 - R_1}\right)^2 \frac{r' - R_1}{r'}. \quad (20)$$

The density is anisotropic, with principal components ρ'_r in the radial direction and ρ'_ϕ in the tangential direction.

Since these material properties are already determined in the principal axes, we can directly apply Eqs. (18) to obtain the polarizabilities along the principal axes in which $|J| = (\kappa')^{-1}$, $\hat{J}_r^* = \rho'_r$, and $\hat{J}_\phi^* = \rho'_\phi$, according to Eq. (17).

In view of the numerical simulations that follow, we express the dipole polarizability tensor in a Cartesian system of coordinates (x', y') by properly rotating the polar coordinates by angle ϕ [51,52]. We obtain the nondiagonal dipole polarizability tensor

$$\hat{\boldsymbol{\alpha}}^{(d)} = \mathbf{Q}^{-1}\boldsymbol{\alpha}^{(d)}\mathbf{Q}, \quad \mathbf{Q} = \begin{bmatrix} \cos\phi & \sin\phi \\ -\sin\phi & \cos\phi \end{bmatrix}, \quad (21)$$

where $\mathbf{Q}$ is the rotation matrix. The physical significance of the nondiagonal elements of $\hat{\boldsymbol{\alpha}}^{(d)}$ is that the dipoles are not aligned along the principal directions of anisotropy and must be sensitive to the particle velocity in all directions, not just along their axes.

The acoustic cloak was simulated using the same source model as the slab simulation of the previous section, but with anisotropic and spatially varying polarizabilities. The chosen geometry was a scatterer of radius $R_1 = 0.6\lambda$ encapsulated by a cloak of radius $R_2 = 2R_1$, both modeled with hexagonally packed source cells [see Fig. 1(a)] spaced $\lambda/50$ apart. This packing method was employed to better approximate the curved geometry. A scatterer with $\kappa_{\text{eff}} = 50$ and $\rho_{\text{eff}} = 50$ was selected so that there would be high contrast between the cloaked and uncloaked pressure fields. The position of the
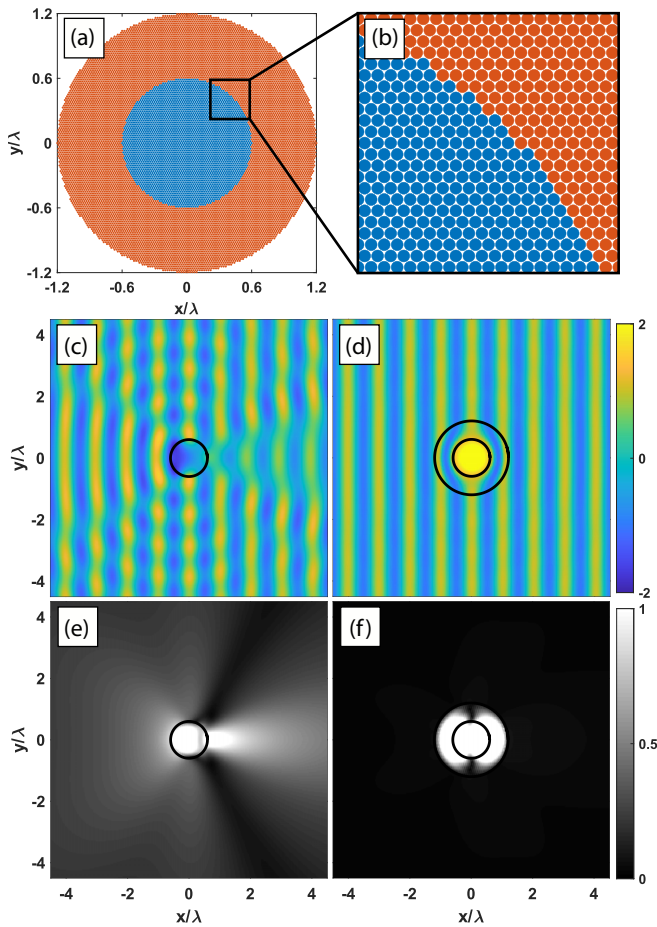
FIG. 3. Demonstration of the source modeling of a cloaked scatterer in a background plane wave in the x direction. The cloak and scatterer are represented with source cells marked by solid circles with spacing of $\lambda/50$ for (a) the full geometry and (b) a zoomed in view. The total pressure is shown for (c) the scatterer and (d) the cloaked scatterer. The normalized scattered pressure magnitude is also shown for (e) the scatterer and (f) the cloaked scatterer.

FIG. 4. Polar plots of the scattered pressure from a cloaked scatterer at a radius of 20λ for varying (a) cloak thickness and (b) unit cell dimension.

source cells used to model the scatterer (blue) and cloak (red) are shown with solid circles in Figs. 3(a) and 3(b).

The results of the simulation for an incident plane wave in the x direction are displayed in Figs. 3(c)–3(f). In Fig. 3(c), the total pressure field for the uncloaked scatterer is shown. A high amplitude reflection region and low amplitude transmission region are clearly visible, with radial scattering above and below. In contrast, only the background plane wave is present outside the cloaking shell in Fig. 3(b). The absence of scattering indicates that the prescribed anisotropy and steep material gradients were accurately represented. Also supporting this is the high curvature of the waves around the inner cloak boundary, which should be expected for the density approaching infinity. In Figs. 3(e) and 3(f), the normalized amplitudes of just the scattered fields are plotted to highlight the effectiveness of the cloak.

It should be expected that the performance deteriorates as the lattice period of the source cell medium and/or the material parameter gradients increase with respect to the wavelength of the external field. This effect was assessed by varying
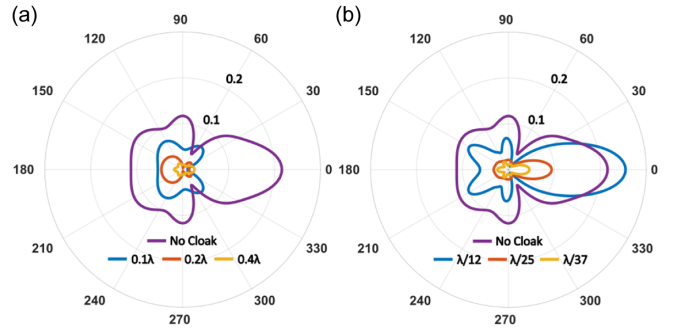
the cloak thickness and unit cell dimension. The results are shown in Fig. 4 as polar plots of the scattered field amplitudes at $r = 20\lambda$. Decreasing the thickness of the cloak steepens the property gradients and reduces the number of cells if spacing is held constant. This results in a highly discretized property curve and a less effective cloak, as shown by the scattered pressure trend in Fig. 4(a). Additionally, a thin cloak may be more heavily impacted by boundary effects, as seen in other homogenized media such as wired electromagnetic metamaterials [53,54]. The polarizabilities of the sources on the boundaries of the structure could potentially be adjusted to account for this and better match the desired material properties. The number of unit cells can be reduced directly by increasing the unit cell dimension, with similar effect on the performance, as shown in Fig. 4(b). The relationships used to calculate the polarizabilities will lose accuracy as the dimension approaches the scale of the wavelength.

An alternate method of studying the effects of the source model is to design a cloak for a single incident wave frequency f_0 and then evaluate its performance over a frequency range. We used the geometry shown in Fig. 3 and as a performance metric chose the ratio of the scattered power with the cloak P_{cloaked} to that without the cloak P_0. While the macroscopic material properties are independent of the incident frequency (assuming no dispersion), the source polarizability amplitudes are not, as their calculation in Eq. (11) includes a k_0 term. We examined cloak performance for both the cases of constant polarizabilities designed for f_0 and varying, frequency dependent polarizabilities. The results are plotted in Fig. 5. It is clear from the steep increase in scattering that, for a cloak to operate outside a very narrow frequency band, it is necessary for the polarizabilities to vary, as their amplitude must depend on frequency. When this is true, the performance approaches the ideal zero scattering as the unit cell dimension becomes increasingly small compared to the wavelength and the first order approximation employed in our derivations becomes more accurate. It should also be noted that the frequency independence of the required polarizability phases violates causality and practical implementation will be constrained to some bandwidth. In general, the parametric studies shown in Figs. 4 and 5 provide useful guidelines for the physical realization of such a cloak with active unit cells and insight
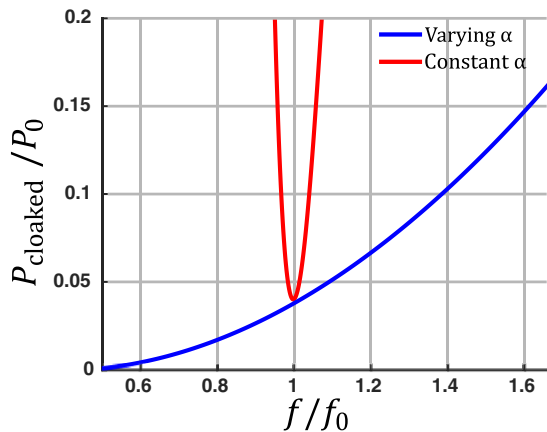
FIG. 5. Cloak performance, quantified by the cloaked scattered power relative to the uncloaked scattered power, is plotted as a function of the frequency of the incident plane wave. The cloak geometry was fixed, but the polarizabilities were either constant or varying with frequency.

into how the performance will compare to the ideal continuous design.

V. CONCLUSION

We derived an analytical method to relate the polarizabilities of media composed of polarized sources separated by significantly subwavelength distances to the macroscopic acoustic properties of acoustically equivalent continuous materials. We considered bulk transformation acoustics media in which the high mass density anisotropy and the steep gradients of bulk modulus and mass density are accurately modeled by collections of unit cells composed of one monopole and two dipole sources whose amplitude and phase is determined by the local acoustic pressure and particle velocity. The polarizabilities of a single cell were first solved for in terms of the relative bulk modulus κ_{cyl} and mass density $\boldsymbol{\rho}_{cyl}$ of a

subwavelength cylinder by equating the expressions for the scattered fields from an incident plane wave. The cylinder properties necessary for the desired effective properties κ_{eff} and $\boldsymbol{\rho}_{eff}$ were then found from the homogenization of an array of cylinders placed in a background fluid. Finally, the set of polarizabilities could be determined directly from the effective properties.

Remarkably, the source polarizabilities inside each cell are related through closed-form expressions to the local effective macroscopic material properties in the equivalent continuous medium. This enabled the application of the source model to transformation acoustics and derivations of the source polarizabilities directly from the underlying coordinate transformations.

The source model was validated by comparing the acoustic fields scattered by several continuous homogeneous and inhomogeneous media and obtained in numerical simulations performed with COMSOL MULTIPHYSICS with the fields scattered by the media realizations with source lattices. In particular, a free space cloak was modeled to exhibit the ability to accurately represent steep material property gradients and anisotropy. The simulated cloak produced almost no scattered field, indicating that the material properties and geometry were accurately represented.

The relationships between the polarizabilities and macroscopic acoustic properties presented in this work will help to enable the development of new active metamaterials using the sensor-driver architecture. With a suitable physical implementation, the effective bulk modulus and mass density tensor should be independently controllable in each unit cell across 2D and 3D bulk geometries. Ultimately, this would provide a path towards realizing general reconfigurable acoustic devices and exciting applications of transformation acoustics such as cloaking.

ACKNOWLEDGMENT

[1] H. Chen and C. T. Chan, Appl. Phys. Lett. **91**, 183518 (2007).

[2] S. A. Cummer and D. Schurig, New J. Phys. **9**, 45 (2007).

[3] A. N. Norris, Proc. R. Soc. A **464**, 2411 (2008).

[4] N. Fang, D. Xi, J. Xu, M. Ambati, W. Srituravanich, C. Sun, and X. Zhang, Nat. Mater. **5**, 452 (2006).

[5] S. H. Lee, C. M. Park, Y. M. Seo, Z. G. Wang, and C. K. Kim, J. Phys.: Condens. Matter **21**, 175704 (2009).

[6] Z. Liu, X. Zhang, Y. Mao, Y. Y. Zhu, Z. Yang, C. T. Chan, and P. Sheng, Science **289**, 1734 (2000).

[7] Y. Ding, Z. Liu, C. Qiu, and J. Shi, Phys. Rev. Lett. **99**, 093904 (2007).

[8] Z. Yang, J. Mei, M. Yang, N. H. Chan, and P. Sheng, Phys. Rev. Lett. **101**, 204301 (2008).

[9] S. H. Lee, C. M. Park, Y. M. Seo, Z. G. Wang, and C. K. Kim, Phys. Lett. A **373**, 4464 (2009).

[10] Z. Liang and J. Li, Phys. Rev. Lett. **108**, 114301 (2012).

[11] Y. Xie, B.-I. Popa, L. Zigoneanu, and S. A. Cummer, Phys. Rev. Lett. **110**, 175501 (2013).

[12] J. B. Pendry and J. Li, New J. Phys. **10**, 115032 (2008).

[13] B.-I. Popa and S. A. Cummer, Phys. Rev. B **80**, 174303 (2009).

[14] S. Zhang, C. Xia, and N. Fang, Phys. Rev. Lett. **106**, 024301 (2011).

[15] L. Zigoneanu, B.-I. Popa, and S. A. Cummer, Phys. Rev. B **84**, 024305 (2011).

[16] S. A. Cummer, J. Christensen, and A. Alù, Nat. Rev. Mater. **1**, 1 (2016).

[17] G. Ma and P. Sheng, Sci. Adv. **2**, e1501595 (2016).

[18] G. Liao, C. Luan, Z. Wang, J. Liu, X. Yao, and J. Fu, Adv. Mater. Technol. **6**, 2000787 (2021).

[19] B.-I. Popa, L. Zigoneanu, and S. A. Cummer, Phys. Rev. Lett. **106**, 253901 (2011).

[20] L. Zigoneanu, B.-I. Popa, and S. A. Cummer, Nat. Mater. **13**, 352 (2014).

[21] Y. Bi, H. Jia, W. Lu, P. Ji, and J. Yang, Sci. Rep. **7**, 705 (2017).

[22] S.-K. Yang, J.-C. Lin, and J.-W. Cheng, Appl. Sci. **7**, 456 (2017).

[23] Y. Chen, M. Zheng, X. Liu, Y. Bi, Z. Sun, P. Xiang, J. Yang, and G. Hu, Phys. Rev. B **95**, 180104(R) (2017).

[24] B.-I. Popa and S. A. Cummer, Microwave Opt. Technol. Lett. **49**, 2574 (2007).

[25] W. Akl and A. Baz, J. Intell. Mater. Syst. Struct. **21**, 541 (2010).

[26] A. M. Baz, J. Vibrat. Acoust. **132**, 041011 (2010).

[27] B.-I. Popa and S. A. Cummer, Phys. Rev. B **85**, 205101 (2012).

[28] W. Akl and A. Baz, J. Appl. Phys. **112**, 084912 (2012).

[29] B.-I. Popa, L. Zigoneanu, and S. A. Cummer, Phys. Rev. B **88**, 024303 (2013).

[30] B.-I. Popa, D. Shinde, A. Konneker, and S. A. Cummer, Phys. Rev. B **91**, 220303(R) (2015).

[31] A. Baz, J. Acoust. Soc. Am. **143**, 1376 (2018).

[32] Y. Chen, X. Li, H. Nassar, G. Hu, and G. Huang, Smart Mater. Struct. **27**, 115011 (2018).

[33] B.-I. Popa, Y. Zhai, and H.-S. Kwon, Nat. Commun. **9**, 5299 (2018).

[34] Y. Zhai, H.-S. Kwon, and B.-I. Popa, Phys. Rev. B **99**, 220301(R) (2019).

[35] A. Sasmal, N. Geib, B.-I. Popa, and K. Grosh, New J. Phys. **22**, 063010 (2020).

[36] N. Geib, A. Sasmal, Z. Wang, Y. Zhai, B.-I. Popa, and K. Grosh, Phys. Rev. B **103**, 165427 (2021).

[37] C. R. Simovski, Metamaterials **1**, 62 (2007).

[38] C. Fietz and G. Shvets, in *Metamaterials: Fundamentals and Applications II* (International Society for Optics and Photonics, Bellingham, WA, 2009), Vol. 7392, p. 73920L.

[39] A. Alù, Phys. Rev. B **84**, 075153 (2011).

[40] J. R. Willis, Proc. R. Soc. A **467**, 1865 (2011).

[41] L. Goltcman and Y. Hadad, Phys. Rev. Lett. **120**, 054301 (2018).

[42] C. F. Sieck, A. Alú, and M. R. Haberman, Phys. Rev. B **96**, 104303 (2017).

[43] H. Esfahlani, Y. Mazor, and A. Alú, Phys. Rev. B **103**, 054306 (2021).

[44] A. Melnikov, Y. K. Chiang, L. Quan, S. Oberst, A. Alù, S. Marburg, and D. Powell, Nat. Commun. **10**, 3148 (2019).

[45] L. Kinsler, C. Alan, J. Sanders, and A. Frey, *Fundamentals of Acoustics*, 4th ed. (John Wiley & Sons, New York, 2000).

[46] D. Torrent and J. Sanchez-Dehesa, Phys. Rev. B **79**, 174104 (2009).

[47] M. B. Muhlestein, B. M. Goldsberry, A. N. Norris, and M. R. Haberman, Proc. R. Soc. A **474**, 20180571 (2018).

[48] V. Fokin, M. Ambati, C. Sun, and X. Zhang, Phys. Rev. B **76**, 144302 (2007).

[49] B.-I. Popa, Phys. Rev. B **96**, 094305 (2017).

[50] S. A. Cummer, in *Acoustic Metamaterials: Negative Refraction, Imaging, Lensing and Cloaking*, edited by R. V. Craster and S. Guenneau, Springer Series in Materials Science (Springer Netherlands, Dordrecht, 2013), pp. 197–218.

[51] S. A. Cummer, B.-I. Popa, D. Schurig, D. R. Smith, and J. Pendry, Phys. Rev. E **74**, 036621 (2006).

[52] A. F. Bower, *Applied Mechanics of Solids* (CRC Press, Boca Raton, FL, 2009).

[53] M. G. Silveirinha, Phys. Rev. B **75**, 115104 (2007).

[54] S. Lannebère, T. A. Morgado, and M. G. Silveirinha, Compt. Rend. Phys. **21**, 367 (2020).